Numerical Simulations of Interactions between Gravity Waves and Deep Moist Convection

ZACHARY A. EITZEN

Atmospheric Sciences, NASA Langley Research Center, Hampton, Virginia, and Department of Atmospheric Science, Colorado State University, Fort Collins, Colorado

DAVID A. RANDALL

Department of Atmospheric Science, Colorado State University, Fort Collins, Colorado

(Manuscript received 19 May 2003, in final form 2 September 2004)

ABSTRACT

This study uses a numerical model to simulate deep convection both in the Tropics over the ocean and the midlatitudes over land. The vertical grid that was used extends into the stratosphere, allowing for the simultaneous examination of the convection and the vertically propagating gravity waves that it generates. A large number of trajectories are used to evaluate the behavior of tracers in the troposphere, and it is found that the tracers can be segregated into different types based upon their position in a diagram of normalized vertical velocity versus displacement. Conditional sampling is also used to identify updrafts in the troposphere and calculate their contribution to the kinetic energy budget of the troposphere. In addition, Fourier analysis is used to characterize the waves in the stratosphere; it was found that the waves simulated in this study have similarities to those observed and simulated by other researchers. Finally, this study examines the wave energy flux as a means to provide a link between the tropospheric behavior of the convection and the strength of the waves in the stratosphere.

1. Introduction

Deep convection is associated with a wide variety of dynamics in the troposphere. These include turbulent eddies that occur on the microscale within convective clouds, gravity waves with a variety of wavelengths that are triggered by convection, and compensating subsidence that can extend hundreds of kilometers from the convective towers. All of these processes are important to the life of the convection and its interaction with the surrounding environment.

Recently, the importance of deep convection to the dynamics of the stratosphere has been identified. In both observational (Clark and Morone 1981; Pfister et al. 1986, 1993; Sato 1993; Dewan et al. 1998) and numerical (Fovell et al. 1992; Pandya and Alexander 1999; Lane et al. 2001) studies, gravity waves have been shown to propagate vertically into the stratosphere above convection. Vertically propagating gravity waves carry a momentum flux that may alter the mean winds above the convection by depositing their momentum at their critical levels (Eliassen and Palm 1960). If no critical level is present for the waves, they may still deposit their momentum once the amplitude increases with height until the atmosphere becomes unstable (Lindzen 1981). Convectively generated gravity waves may carry a momentum flux of similar magnitude to that of orographically generated waves (Fritts and Nastrom 1992), which have long been acknowledged as important to the flow for altitudes within and above the upper troposphere (Bretherton 1969). Researchers such as Dunkerton (1997) have identified vertically propagating convectively generated gravity waves as being important for the maintenance of the quasi-biennial oscillation (QBO; Baldwin et al. 2001). Therefore, a treatment of convectively generated gravity waves is an important goal for climate models.

Two techniques that have been used in the past to analyze convective processes are Lagrangian trajectories and conditional sampling. Several authors have used Lagrangian trajectories to diagnose the entrainment of dry air by clouds, including Reuter and Yau (1987) and Lin and Arakawa (1997). In the Reuter and Yau (1987) study, several trajectories that illustrated different types of cloud entrainment processes were analyzed. The authors kept track of fields such as height, liquid water mixing ratio, and the equivalent potential temperature along the trajectories' paths. In

Corresponding author address: Zachary A. Eitzen, Mail Stop 420, NASA Langley Research Center, Hampton, VA 23681-2199.
E-mail: z.a.eitzen@larc.nasa.gov

the Lin and Arakawa (1997) study, the authors computed backward trajectories for many cloudy parcels to determine where they came from and how fields such as the total water mixing ratio and moist static energy varied along these trajectories' paths.

Conditional sampling has also been used by many previous authors. LeMone and Zipser (1980) and Zipser and LeMone (1980) used vertical velocity data obtained from flights during the Global Atmospheric Research Programme's (GARP) Atlantic Tropical Experiment (GATE) to diagnose turbulent updrafts and updraft cores. Greenhut and Khalsa (1982) diagnosed updrafts and downdrafts within the boundary layer over the Pacific Ocean, using aircraft measurements of the vertical velocity, and then normalized this quantity with a mixed-layer vertical velocity scale. In Williams et al. (1995), the authors classified precipitating clouds into several categories (deep convective, shallow convective, stratiform, and mixed stratiform/convective) based on observations of the vertical structures of reflectivity, vertical velocity, and turbulence that were obtained with a wind profiler.

The Arakawa–Schubert (1974; see also Schubert 2000) cumulus parameterization is a way to account for the effects of subgrid-scale cumuli in large-scale models. Since there is typically an ensemble of shallow and deep cumuli coexisting within the area represented by a single grid cell, each cloud-top height is associated with a separate "type," or subensemble. Since the heating and drying effects of cumulus convection can be determined in terms of a mass flux into the cumuli, we need to determine this mass flux. More details of this formulation will be explored later, where a measure of the effect of the gravity waves on the convection will be shown.

In this paper, we will examine the use of particle trajectories to diagnose the behavior of air parcels in numerical simulations of convection. This analysis plots thousands of trajectories on a new type of diagram that plots displacement versus a normalized vertical velocity. We will also use conditional sampling to identify moist updrafts in a systematic manner, with selection criteria based on the results of the trajectory simulations. This section explores the amount of perturbation kinetic energy associated with horizontal and vertical motions, as well as the difference in horizontal wind speed between the updrafts and the mean wind. Fourier analysis and trajectories will then be used to characterize the motions in the stratosphere, which are dominated by gravity waves with a wide range of phase speeds. Finally, we will discuss the behavior of the wave energy flux in the troposphere and stratosphere, and discuss the impact that this flux may have on the convection itself in the context of the Arakawa–Schubert cumulus parameterization.

2. Model

The model that was used to perform the simulations analyzed in this study is the two-dimensional version of the Advanced Regional Prediction System (ARPS). The dynamics and physics of this model are summarized in Xue et al. (2000) and Xue et al. (2001), respectively. ARPS has been used by Robe and Emanuel (2001) to study radiative–convective equilibrium, and also in an idealized study of thunderstorm outflows (Haertel et al. 2001). Briefly, the model features elastic dynamics, Kessler (1969) warm rain, and Lin et al. (1983) ice microphysics. The model solves for the terms that are associated with acoustic waves on a short time step, and all other terms on a long time step, using the mode-splitting technique described in Klemp and Wilhelmson (1978). A radiation parameterization is available in ARPS, but was not used in this study, because of its relatively low importance in the development of simulated squall lines (Redelsperger et al. 2000).

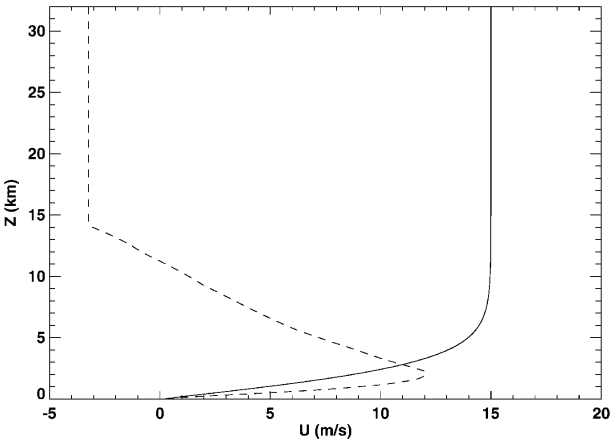

FIG. 1. Plot of the initial wind profile used in the WK run (solid line), and the TC run (dashed line) relative to the ground. To obtain the winds relative to the computational domains, subtract speeds of 16 and 12 m s^{-1} from the WK and TC runs, respectively.

The cases analyzed here are two-dimensional representations of squall lines. The first (hereafter, WK) uses the analytic sounding of Weisman and Klemp (1982), which is based on observations of midlatitude squall lines in the Great Plains of the United States. The convective available potential energy (CAPE) associated with this sounding was 2650 J kg^{-1}, calculated according to the method described in Emanuel (1994), using code provided by K. Emanuel (2001, personal communication). The wind profile (see Fig. 1) used in the WK run has most of its shear in the lowest 3 km of the atmosphere, which is consistent with the statement by Rotunno et al. (1988) that strong low-level shear is necessary for long-lived squall lines. The domain moved at 16 m s^{-1}, in order to keep the storm approximately centered. For this simulation, we used a grid with uniform spacings of 1 km in the horizontal, and 250 m in the vertical. The extent of the domain was 900 km in the horizontal, and 48 km in the vertical. The horizontal boundary conditions are periodic. This simulation was initialized with a surface cold anomaly. The WK simu-

lation lasted 10 h. The layers in the top 16 km of the vertical domain were a sponge region, which was present to suppress the reflection of waves from the upper boundary. The surface physics used in the model are described in Xue et al. (2001). We performed another numerical experiment in which the same thermodynamic sounding was used as the WK run, but with no wind (a thermal bubble was used for initiation in this case). This run is denoted as the WK calm run. For the WK experiments, we used constant drag coefficients for the parameterization of surface momentum and moisture fluxes.

The second case, called TC, used a sounding observed over the tropical western Pacific Ocean during the Tropical Ocean Global Atmosphere Coupled Ocean–Atmosphere Response Experiment (TOGA COARE), as described by Redelsperger et al. (2000; see also Jorgensen et al. 1997; Trier et al. 1996). The CAPE associated with this sounding was 2210 J kg^{-1}. The winds correspond to a westerly jet (see Fig. 1), which is commonly observed with tropical squall lines (Jorgensen et al. 1997). In this case, the domain propagated at 12 m s^{-1}. The horizontal grid spacing was 500 m, following Nicholls et al. (1988), who found that very fine resolution in the horizontal was necessary to simulate tropical squall lines in 2D. The horizontal domain in the TC runs was 600 km wide, with periodic boundary conditions. A stretched vertical grid was used in the lowest 2500 m of the TC runs, consistent with the guidance of Redelsperger et al. (2000), who noted that the cold pool associated with this convective system is quite shallow. The grid spacing ranged from 71 m near the surface to a constant value of 258 m above 2500 m. The convection was initiated with cooling and drying tendencies following Redelsperger et al. (2000), and the simulation lasted for 8.5 h. The drag coefficients were allowed to depend upon stability because of the importance of accurately simulating the surface moisture flux in the tropical ocean environment.

For both the WK and TC runs, an isothermal stratosphere was assumed, with a constant temperature above 12 km for the WK simulations, and a constant temperature above 19 km in the TC simulation. This also means that the Brunt–Väisälä frequency is constant in the model stratospheres of these simulations. There are many other cases that have been analyzed that will not be presented in this paper. For more information about these cases, see Eitzen (2001).

3. Tropospheric motions

a. Lagrangian trajectories

ARPS stores the velocity fields at three time levels, spanning an interval of 8 s, or twice the long time step for all of the simulations presented in this study. These velocities were used to construct the background winds for the particles. The method used to advect the particles is the fourth-order Runge–Kutta scheme, similar to that used by Krueger et al. (1995).

To calculate particle trajectories, we also need to have values of u and w at each particle's location. This was accomplished by performing a linear interpolation of these quantities to the position of the particle from surrounding grid points. In addition to calculating the position and speed of the particles, we can also interpolate the values of other scalar variables to the particles' positions. Once the trajectories are obtained, statistics can be calculated for the particles, some of which can be combined in an attempt to separate convective motions from nonconvective motions (including gravity waves). One such statistic is a normalized mean vertical velocity given by

$$\hat{w} = \frac{\overline{w}}{\overline{(w^2)}^{1/2}}. \tag{1}$$

Note that in this case, the overbar denotes a time average along the particle's path. The value of $\hat{w}$ will be 1 for a particle that experiences upward vertical velocity that is constant in time, -1 for a particle that experiences downward vertical velocity that is constant in time, and 0 for particles with oscillatory or no vertical motion. The magnitude of a particle's displacement over the time period of the trajectory integration can be determined by calculating

$$\delta z = z_{\max} - z_{\min}, \tag{2}$$

where $z_{\max}$ and $z_{\min}$ are the maximum and minimum altitudes of the particle, respectively. Finally, we will also calculate the average cloud condensate (liquid water plus ice) $\overline{q_c}$ along each particle's path.

A plot of these three variables for the WK run at $t =$ 3 h is shown in Fig. 2a. The particles shown in this figure were initially placed at all of the points where scalar variables are defined throughout the model troposphere (the lowest 12 km), and then advected for 30 min. This time interval was chosen because it is long enough for particles to travel great vertical distances, but short enough so that not too many particles experience both convective and nonconvective motions, which would hamper separation. Physical interpretations can be made for several of the "regions" in the plot. The trajectories with the largest displacements also move up, on average, and are cloudy as well, indicating that these particles can be associated with moist convective updrafts. The many particles that have displacements of 50 to 500 m and a normalized vertical velocity near -1 are affected by the slow compensating subsidence outside of the storm. The particles with significant displacements and a normalized vertical velocity near zero are undergoing a short-period wave or turbulent motions, oscillating about their initial positions. Note that nearly all of the particles with large-amplitude displacements also have $\hat{w} > 0$ and $\overline{q_c} > 10^{-2}$ g kg^{-1}. In fact, most of the particles in the moist up-

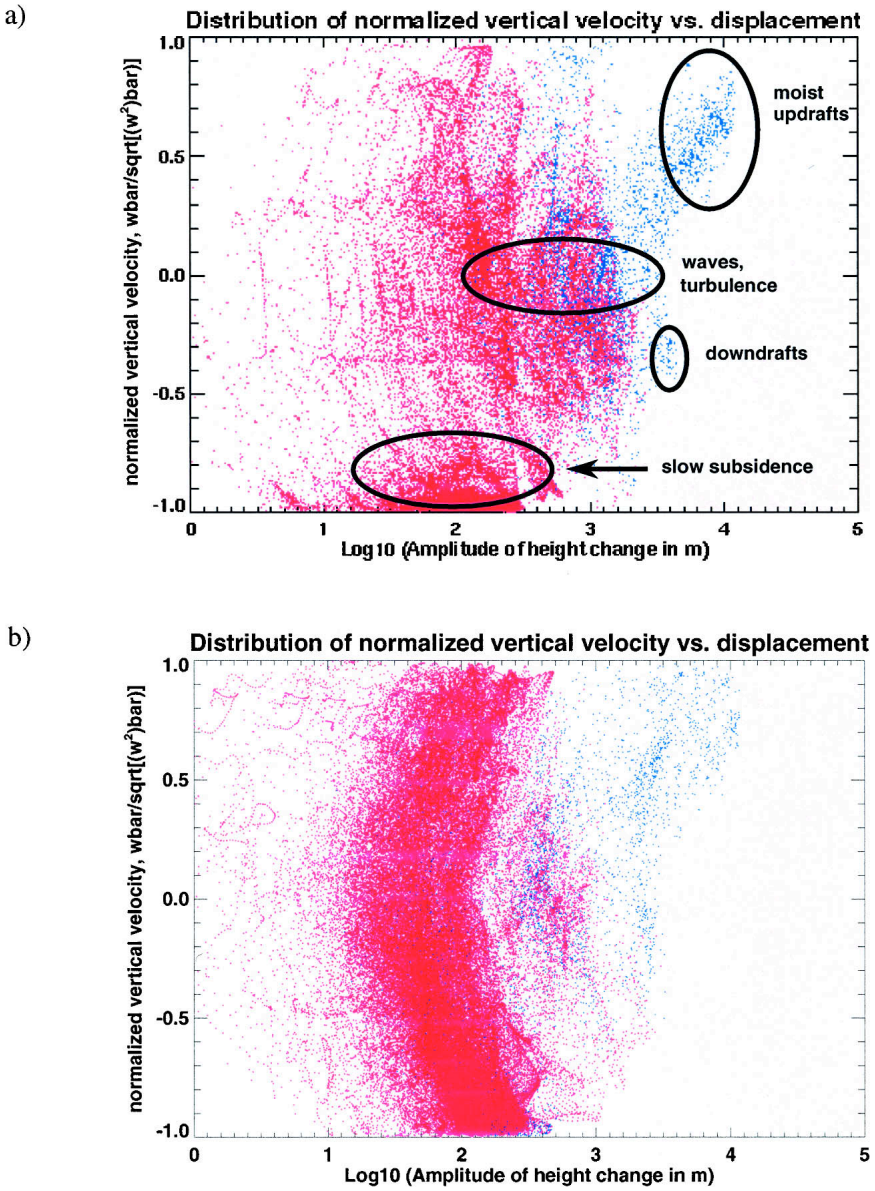

FIG. 2. Plot of normalized vertical velocity defined in (1) vs the $\log_{10}$ of displacement for particles that have been advected for 30 min (a) in the WK run, starting at $t = 3$ h, and (b) in the TC run, starting at $t = 6.5$ h. The red "dry" particles have $\overline{q_c} < 10^{-2}$ g kg^{-1}, while the blue "wet" particles have $\overline{q_c} > 10^{-2}$ g kg^{-1}.

drafts category have $\overline{q_c} > 10^{-1}$ g kg^{-1}, whereas the few downdraft particles have 10^{-1} g kg^{-1} $\geq \overline{q_c} > 10^{-2}$ g kg^{-1}. The reason that there are few convective downdrafts in this simulation may be because it was performed in two dimensions (Haertel and Johnson 2000).

Several trajectories are shown in Figs. 3a, 3b, and 3c for the moist updraft, waves and turbulence, and slow subsidence categories depicted in Fig. 2, respectively. The moist updraft trajectories generally move along a slanted path. This corresponds to the orientation of the storm itself, as we will see later. It is interesting to note that some air (represented by the blue trajectory in Fig. 3a) moves eastward after undergoing its ascent. Figure 3b shows that some of the particles classified as undergoing wave and turbulent motions experience violent motions (the red trajectory), while others trace relatively smooth, orbitlike trajectories (the green trajectory). Finally, the slow subsidence trajectories shown in Fig. 3c are associated with particles that underwent steady, downward motion to the west and east of the storm.

Similar statistics were computed in the troposphere (the lowest 19 km) of the TC run, with a start time 6.5 h into the simulation, which was a time of strong con-

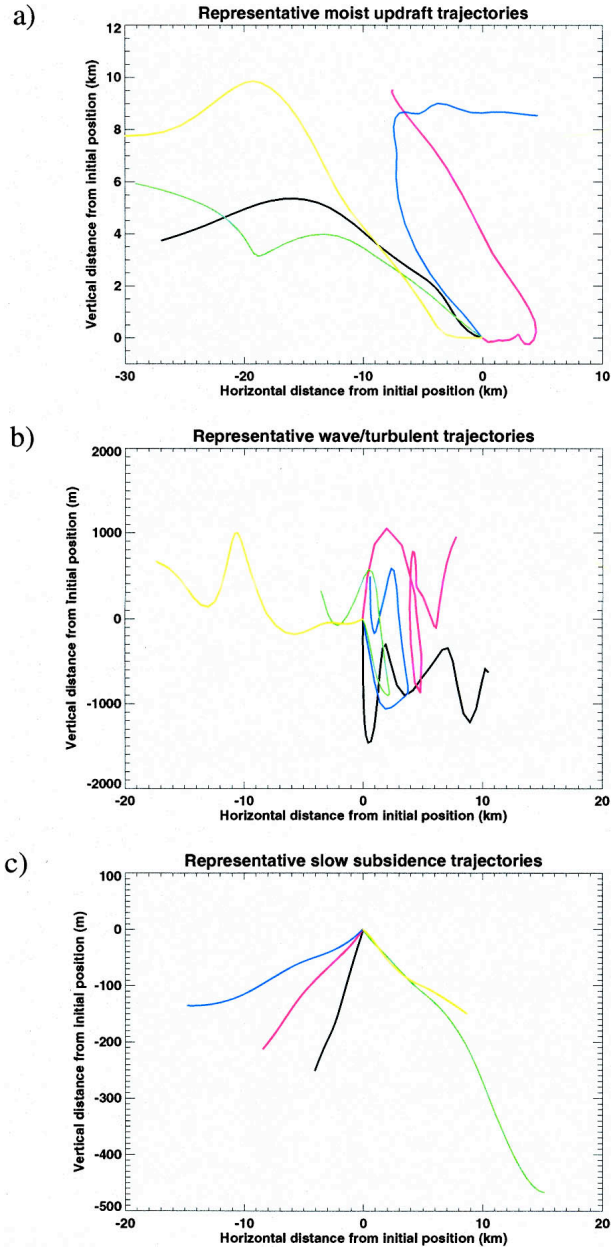

FIG. 3. Plot of particle displacement for three sets of five trajectories classified as (a) moist updrafts, (b) experiencing wave and turbulent motions, and (c) experiencing slow subsidence in Fig. 2. The displacements are normalized so that the initial positions are all at (0, 0), and particle paths can be followed outward from that point.

vection. The results are shown in Fig. 2b. Some of the qualitative features of Fig. 2a are repeated in this figure, particularly in the category of moist updrafts. However, there are apparently more particles that experience slow, steady upward motion (i.e., low-amplitude height change with $\hat{w} > 0.5$). These particles appear to be associated with deep, long-period gravity waves in the troposphere, as seen in Fig. 4. Aside from the vertical motion associated with the convection itself, there are also areas with $\hat{w} > 0.5$ in the boundary layer and in the free troposphere, propagating away from the convection.

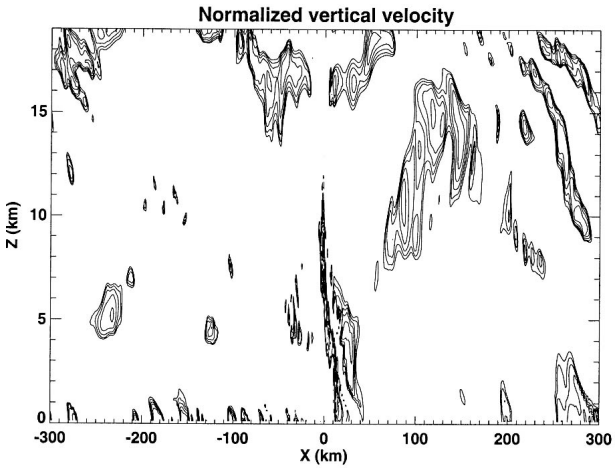

FIG. 4. Locations of upward vertical motion in the troposphere of the TC run. Contours are of normalized vertical velocity greater than or equal to 0.5, with an interval of 0.1. The locations correspond to the initial locations of the particles.

It appears that moist updrafts can be isolated by using the following criteria:

$$\hat{w} > 0,$$
$$\delta z > 2000 \text{ m},$$
$$\overline{q_c} > 10^{-1} \text{ g kg}^{-1}. \quad (3)$$

These criteria, obtained in a Lagrangian framework, give us criteria to classify updraft grid cells in a Eulerian framework. Note that the $\delta z > 2000$ m condition for a 30-min integration is approximately equivalent to $w > 1 \text{ m s}^{-1}$.

b. Conditional sampling

Another technique for identifying cloudy and updraft particles is to analyze snapshots of the storm evolution. If the location of a data point has sufficient condensate ($q_c > 10^{-1}$ g kg^{-1}) to be a cloudy particle at the time of the snapshot, then that location is assigned a "cloud mask" value of 1. Otherwise, the cloud mask has a value of 0. The contribution of cloudy grid points to the covariances or variance of a quantity can then be calculated at each vertical level according to the sum

$$(\overline{a'b'})_{\text{clouds}} = \frac{1}{nx} \sum_{i=1}^{nx} \text{CM}_i a_i' b_i'. \quad (4)$$

Here, CM_i is the value of the cloud mask at the ith location, a' and b' are the departures of the variables a and b from the horizontal mean, and nx is the total

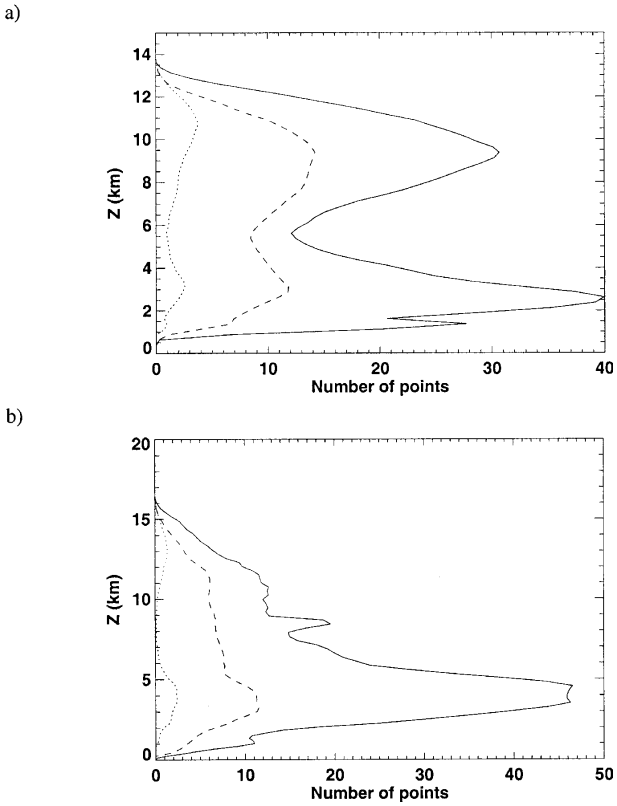

FIG. 5. Plot of the time-averaged number of cloudy points (solid line), updraft points (dashed line), and downdraft points (dotted line) at each vertical level (a) in the WK run, and (b) in the TC run.

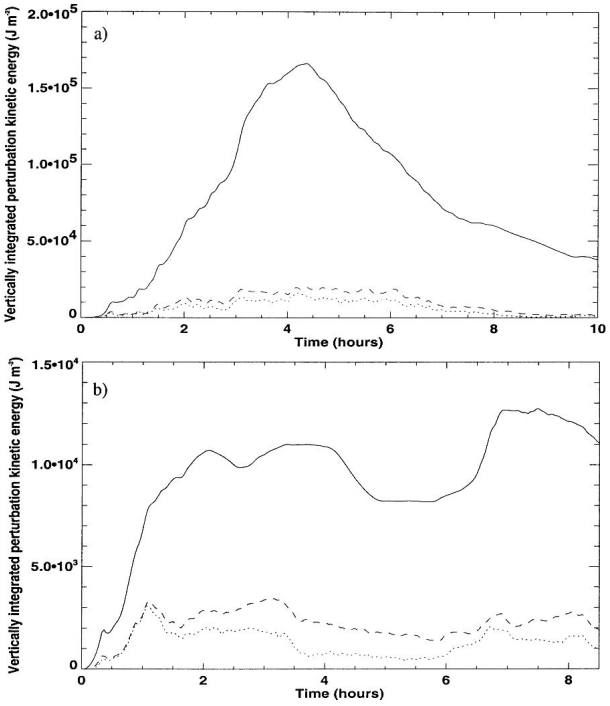

FIG. 6. Vertically integrated perturbation kinetic energy of the troposphere vs time for all points (solid line), cloudy points (dashed line), and updraft points (dotted line) (a) in the WK run, and (b) in the TC run.

number of points in the x direction. When (4) is a variance calculation, $a = b$.

Similarly, the criteria for the updraft mask (UM) includes the condensate concentration, as well as a vertical velocity threshold, that is,

$$\mathrm{UM}_i = \begin{cases} 1 \text{ if } q_c > 10^{-1} \text{ g kg}^{-1} \quad \text{and} \quad w > 1 \text{ m s}^{-1}; \\ 0 \text{ otherwise.} \end{cases} \tag{5}$$

Note that updraft points are a subset of cloudy points according to the above criteria. In addition, these points have values of cloud water and vertical velocity that are similar to those used to identify the moist updraft trajectories described in the previous section. The downdraft points were calculated using a mask similar to that of (5), except with $w < -1$ m s^{-1}.

The time-averaged numbers of cloudy points, updraft points, and downdraft points are shown as functions of height in Figs. 5a and 5b, for the WK and TC runs, respectively. The averages were taken over the lengths of each simulation. In both plots, there are fewer downdraft points than updraft points, which is consistent with the results from the trajectory analysis of the previous section. Note that the grid spacing in the WK run (1000 m) is twice that of the TC run. Updraft and downdraft points are most prevalent in the upper troposphere for the WK run and in the lower troposphere of the TC run. There is also a secondary maximum in the lower troposphere in the WK run. In the WK run, the fields approach zero at an altitude of approximately 13.5 km, which is well above the tropopause at 12 km. This indicates that the convection overshoots the tropopause in this simulation. On the other hand, the convection does not overshoot the higher (19 km) tropopause in the TC run.

When the perturbation kinetic energy, defined by

$$\frac{1}{2}\rho_0(\overline{u'u'} + \overline{w'w'}), \tag{6}$$

is vertically integrated throughout the troposphere, a measure of the amount of the average perturbation kinetic energy contained in a troposphere-deep 1-m^2 column is obtained. The vertically integrated perturbation kinetic energy, with the cloud and updraft masks, is plotted as a function of time in Figs. 6a,b. The perturbation kinetic energy associated with cloudy and updraft points is only a small fraction of the overall perturbation kinetic energy for both simulations. However, the updraft points comprise the majority of this fraction.

Figure 7 shows the component of perturbation ki-

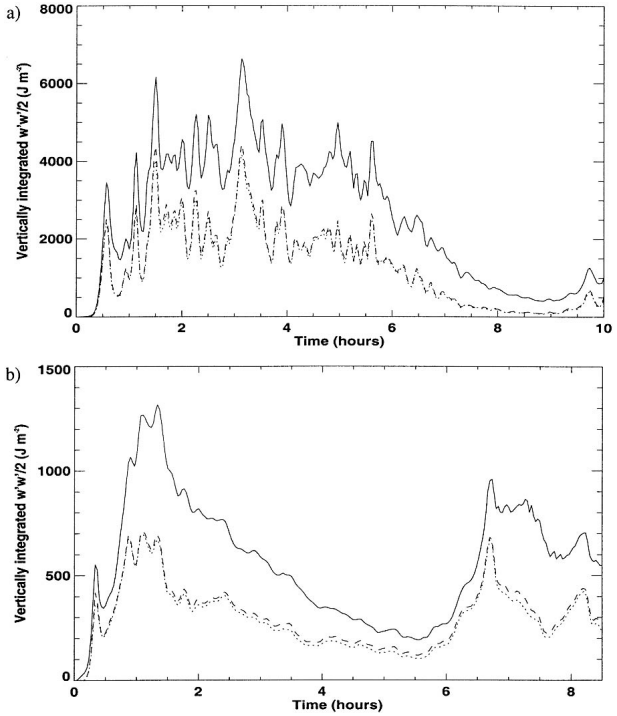

FIG. 7. Vertically integrated perturbation kinetic energy of the troposphere due to vertical motions vs time for all points (solid line), cloudy points (dashed line), and updraft points (dotted line) (a) in the WK run, and (b) in the TC run.

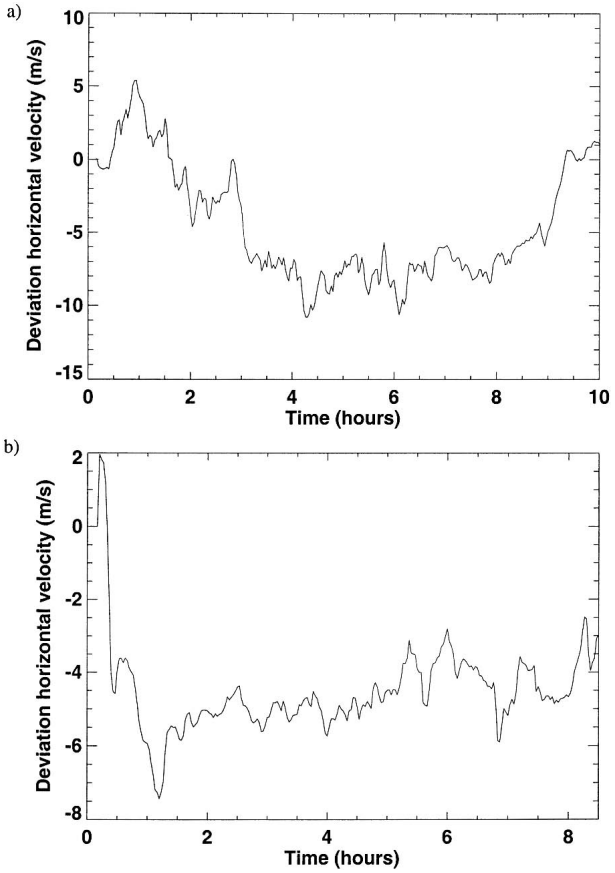

FIG. 8. Comparison of the average difference between the horizontal velocity of the updraft-masked points and that of the mean flow (a) in the WK run, and (b) in the TC run.

netic energy due to vertical motion, $\rho_0 \overline{w'w'}/2$, for all points, cloudy points, and updraft points. The cloudy and updraft points are responsible for a significant portion of the overall vertical perturbation kinetic energy, and the maxima in this portion are highly correlated to the overall vertical perturbation kinetic energy. The vast majority of the $\overline{w'w'}$ due to cloudy points is contained in the updraft points. This is in spite of the fact that there are significantly more cloudy points than updraft points, on average, as shown in Fig. 5.

As we can see from a comparison of Figs. 6 and 7, the horizontal portion of the overall perturbation kinetic energy field is dominant for the entire domain for both simulations. This is consistent with the results of Xu et al. (1992), who found that the horizontal perturbation kinetic energy simulated in their cloud ensemble model was considerably stronger than the vertical perturbation kinetic energy.

Another quantity that is of interest is the extent to which the moist convective updrafts represent an obstacle to the mean flow. Such an obstacle can be considered a "transient mountain" poking into a mean flow, as introduced by Pfister et al. (1993). Note that Pfister et al. (1993) looked at the flow past mesoscale anvils rather than updrafts, so this represents a modified version of their hypothesis. One way to characterize the obstacle that the convection poses to the mean flow is to calculate the difference between u at each updraft point and $\overline{u}$ at that particle's vertical level, and then average over the updraft particles:

$$u'_{\text{up}} = \frac{1}{n_{\text{up}}} \sum_{i=1}^{n_{\text{up}}} u(x_i, z_i) - \overline{u}(z_i). \tag{7}$$

The WK run begins with the updrafts having winds that are more westerly (downshear) than those of the surrounding atmosphere, and then becoming more easterly (upshear) with time as shown in Fig. 8a. This is also consistent with the production of more eastward-propagating waves earlier in the WK run. This evolution can be seen by comparing a plot of potential temperature surfaces above the convection after 2 h (Fig. 9a) with plots taken at later times (Figs. 9b–d). The evolution of the TC run is somewhat similar, but with an earlier and more pronounced rearward tilt than the WK run. The difference between the u of the updrafts and $\overline{u}$ was also tested for the TC run, shown in Fig. 8b. This figure shows that there are significant differences in how u'_{up} evolves with time between these two simulations. In the TC run, we see that after a short period with $u'_{\text{up}} > 0$, the sign of this quantity is consistently

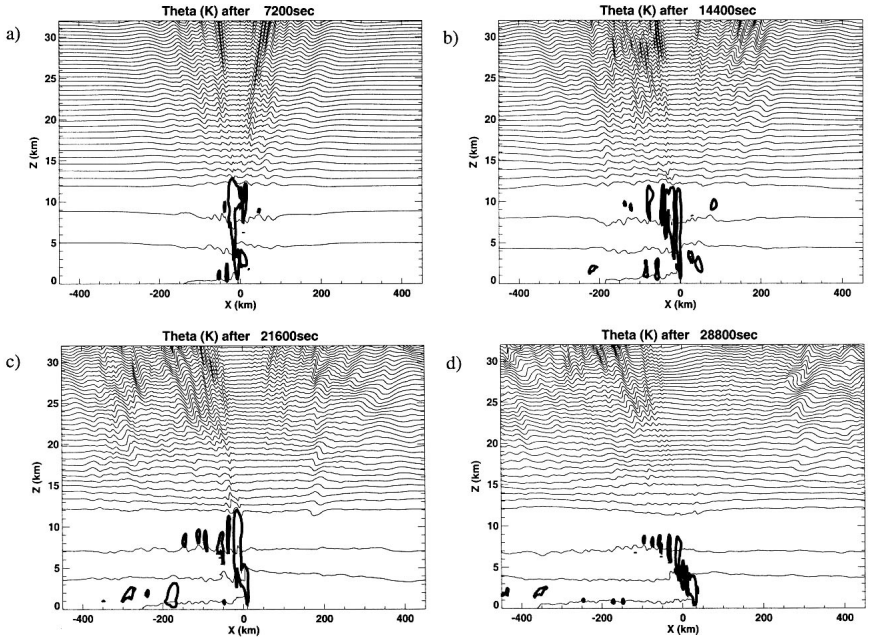

FIG. 9. Potential temperature contoured at 15-K intervals for the WK run after (a) 2, (b) 4, (c) 6, and (d) 8 h. The thick contour encloses cloud condensate greater than 0.1 g kg^{-1}.

negative, as we would expect from a rearward-tilting squall line.

These results indicate that the diagnosis of a quantity such as u'_{up} in cumulus parameterizations may assist researchers that wish to formulate a parameterization for convectively generated gravity waves. Since $u'_{up} < 0$ for the majority of the WK and TC simulations, we should expect more wave momentum flux to be associated with negative phase speeds than positive phase speeds according to the modified Pfister et al. (1993) transient mountain hypothesis. Note that since the updrafts are transient, we do not necessarily expect there to be a peak in the phase speed spectrum located at u'_{up}. Making a quantitative diagnosis of the phase speed spectrum created by updrafts with a given u'_{up} (in addition to other quantities) is an interesting topic for future research.

4. Waves in the stratosphere

We can also use the particle analysis of section 3a to examine what happens in the model stratosphere. In this case, we allowed the particles to be advected for two hours, since we expect the motion in the stratosphere to be dominated by gravity waves, eliminating the need to limit the time of integration to identify the type of motion that each trajectory undergoes. Since the stratosphere is dominated by wave motion, we expect particles undergoing wave motions with periods that are short in comparison to the integration time of the trajectories to have $|\hat{w}| \ll 1$, while particles that undergo long-period wave motion could have $|\hat{w}| \sim 1$. After performing this analysis, we saw that most of the particles released in the WK run starting at $t = 3$ h apparently underwent wave motion (with $|\hat{w}| \sim 0$) in the model stratosphere with a period less than 2 h. This is not an unexpected result since, as we will see later in this section, a Fourier analysis of the motions in the stratosphere shows that most of the waves in the stratosphere had periods of 10 to 60 min. The stratospheric trajectory experiment was also carried out for the TC run. The particles in this simulation tended to have small values of $|\hat{w}|$, like the WK run. However, the particles advected in the TC run underwent much smaller vertical displacements, with most of the displacements clustered around 200 to 400 m. This is consistent with the magnitude of isentropic displacements measured over a tropical mesoscale convective system (MCS) by Pfister et al. (1993).

In this section, we will apply Fourier analysis to the perturbation zonal and vertical velocities. Here, we define a perturbation as a departure from the zonal mean at each time. Specifically, we perform two-dimensional fast Fourier transforms (FFTs) to calculate the spectral density associated with each discrete frequency ω and wavenumber k. The FFTs were performed in a manner such that ω could take on positive or negative values, but $k > 0$. Since the model output was saved every 2 min, the minimum resolved wave period was 4 min, and the minimum resolvable wavelength was 2 km for the WK runs, and 1 km for the TC run.

The intrinsic frequency of the waves relative to the moving air is given by $\omega_{int} = \omega - k\bar{u}$. The normalized power spectrum versus the absolute value of intrinsic

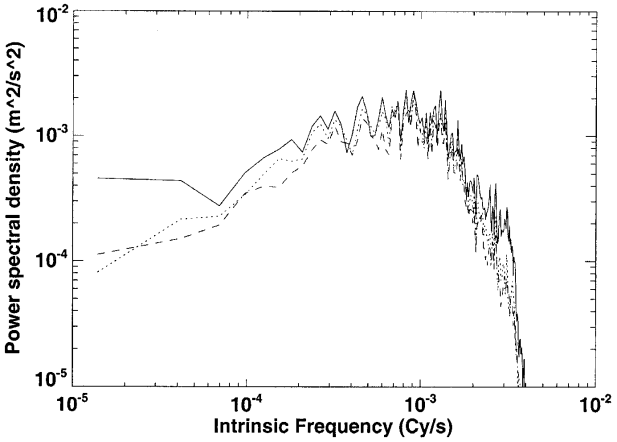

FIG. 10. Log–log plot of the normalized power spectra of vertical velocity at 14 125 m (solid), 21 125 m (dotted), and 28 125 m (dashed) as a function of intrinsic frequency for the WK run.

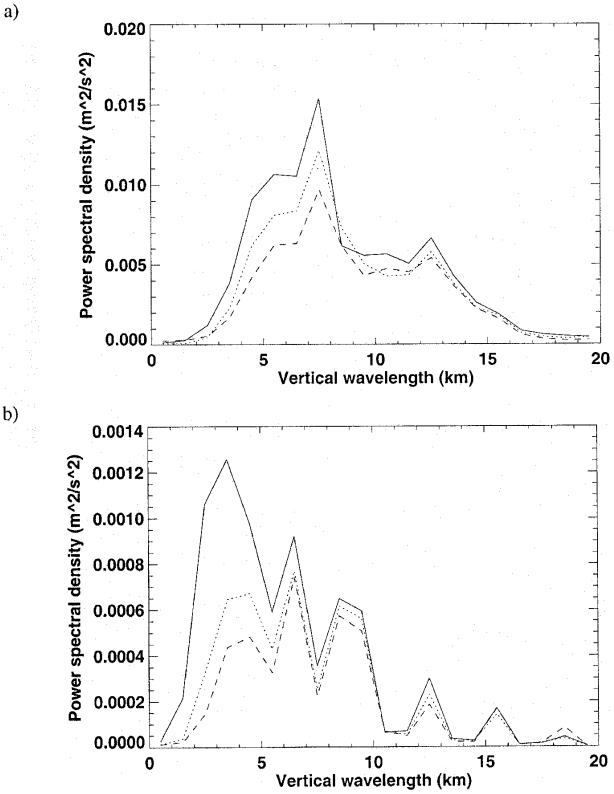

FIG. 11. Plot of the normalized power spectra of vertical velocity as a function of vertical wavelength (a) for the WK run at 14 125 m (solid), 21 125 m (dotted), and 28 125 m (dashed) and (b) for the TC run at 19 255 m (solid), 24 927 m (dotted), and 29 825 m (dashed).

frequency at 14 125, 21 125, and 28 125 m is shown in Fig. 10. These altitudes were chosen to represent the lower, middle, and upper portion of the region between the model tropopause (at 12 km) and the sponge layer (at 32 km). As noted in Hines (1960), vertically propagating gravity waves increase in amplitude with height in proportion to the inverse square root of density. Therefore, in the absence of all other factors, we would expect the variance spectrum at $z = 14\ 125$ m to be replicated at higher altitudes when the spectrum is normalized by multiplying by a factor of $\rho_0(z)/\rho_0$ (14 125 m). Here, we use cycles per second to facilitate comparisons with previous studies (Alexander et al. 1995; Pandya and Alexander 1999, hereafter PA99). A broad peak is seen at frequencies between 0.00025 and 0.0015 cps, which corresponds to periods between about 10 and 60 min. The highest amplitude peak corresponds to a period of 18 min. The overall spectrum is similar in shape to that calculated by PA99, although the highest peak in their frequency spectrum is more prominent than that of Fig. 10. We see that the locations of many of the frequency peaks are maintained with height. However, there is a slight decrease in the (normalized) amplitude of the spectra with height. One possible reason for this decrease is that the model atmosphere at 14 125 m experiences wave motions prior to (and for a longer duration than) the model atmosphere at higher altitudes because of its proximity to the convection and the finite vertical group velocity of the waves. Another explanation is the presence of diffusive damping, which would explain the significant decrease in spectral power at the highest frequencies. The application of a taper function [taken from Percival and Walden (1993)] on the time series had very little effect on the spectrum (not shown). We will refrain from using a taper for the remainder of this section. A similar analysis was carried out for the power spectrum versus horizontal wavenumber, where we found most of the spectral power confined to a broad peak corresponding to wavelengths of 10 to 100 km (not shown).

Another quantity that is interesting to examine is the vertical wavenumber, m. Although this can be calculated directly via FFTs, we have used the linear phase relationship given by

$$m^2 = \frac{k^2N^2}{(\omega - k\bar{u})^2} - \left(k^2 + \frac{1}{4H^2}\right) \tag{8}$$

to assign a value of vertical wavelength $\lambda_z = 2\pi/m$ for each point in (ω, k) space that the spectral density was calculated. The spectral density is then binned in terms of λ_z. The Brunt–Väisälä frequency is given by N, and $H = RT_0/g$ is a scale height, where T_0 is the temperature of the atmosphere. The distribution of the spectral density is shown in Fig. 11a in terms of the vertical wavelength, with a bin width of 1 km. In this figure, we see that there is a peak near $\lambda_z = 8$ km, which is similar to the results of Alexander et al. (1995) and PA99 for similar simulations, as well as Piani et al. (2000) for a somewhat different simulation. These authors attributed the vertical wavelength of the waves to the depth

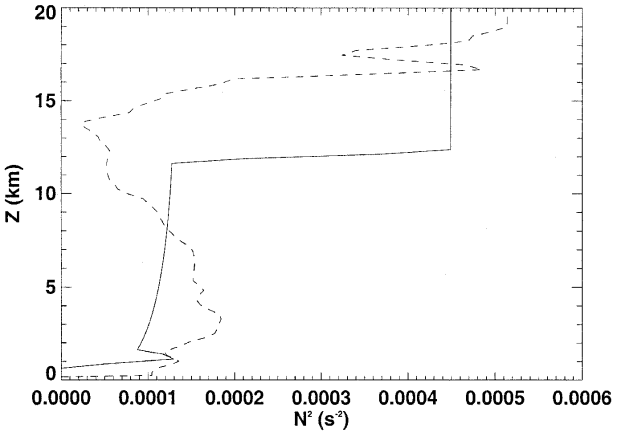

FIG. 12. The square of the Brunt–Väisälä frequency vs height for the WK (solid line) and TC (dashed line) runs.

of the convective heating, consistent with the theoretical results of Salby and Garcia (1987), Nicholls et al. (1991), and Pandya et al. (1993). Since the Brunt–Väisälä frequency roughly doubles between the troposphere and stratosphere (see Fig. 12), tropospheric waves with a half-wavelength of ~8 km (roughly corresponding to the depth of the strongest heating in the WK run) have $\lambda_z \sim 8$ km once they propagate into the stratosphere, according to (8). The fairly sharp peak in Fig. 11a may exist because the convection in the WK run has a fairly consistent structure throughout the simulation.

The convection in the TC run was weaker and more intermittent than that of the WK run. In Fig. 11b, we see a considerably broader spectrum of vertical wavelengths than we saw in Fig. 11a. However, there is significant power for vertical wavelengths of approximately 3 km, probably because the convection had a similar depth for a significant portion of the simulation. Alexander and Holton (1997) also reported a broad spectrum of vertical wavelengths in their simulations of a West African squall line.

The vertical group velocity spectrum c_{gz} can also be obtained, following a similar procedure to the one we used to get the vertical wavenumber spectrum. In Fig. 13a, we see that the power spectrum is distributed across a fairly broad range of c_{gz}, with a peak around 5 m s^{-1}. The energy associated with waves that have a vertical group velocity of 5 m s^{-1} takes a little over an hour to traverse the 20-km-deep model stratosphere. Note that the waves with lower group velocities are damped more than those with higher group velocities as they propagate vertically. This makes sense, since these waves have a longer period of time over which damping processes can affect them.

We expect the waves depicted in Fig. 11b to have smaller vertical group velocities. This is because the equation for group velocity, given by

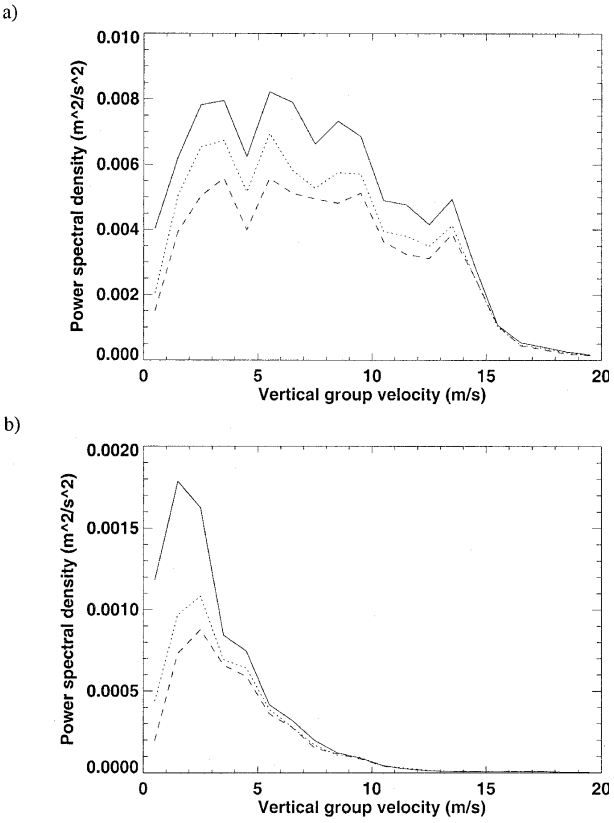

FIG. 13. Plot of the normalized power spectra of vertical velocity as a function of vertical group velocity (a) for the WK run at 14 125 m (solid), 21 125 m (dotted), and 28 125 m (dashed) and (b) for the TC run at 19 255 m (solid), 24 927 m (dotted), and 29 825 m (dashed).

$$c_{gz} = \frac{\partial \omega}{\partial m} = \mp \frac{Nkm}{\left(k^2 + m^2 + \frac{1}{4H^2}\right)^{3/2}}, \tag{9}$$

indicates that c_{gz} is approximately proportional to the square of the vertical wavelength. As we see in Fig. 13b, the waves in the TC run do indeed propagate more slowly in the vertical than those of the WK run. As with the WK run, we see the strongest dissipation with height among the waves with the slowest vertical group velocities.

The cospectrum is defined for two time- and space-varying functions $f(x, t)$ and $g(x, t)$ in terms of phase Φ and amplitude W in the following manner (Hartmann 2004):

$$C_{k,\pm\omega}(f, g) = \frac{1}{2}[W_{k,\pm\omega}(f)][W_{k,\pm\omega}(g)]\cos[\Phi_{k,\pm\omega}(g) - \Phi_{k,\pm\omega}(f)]. \tag{10}$$

The cospectrum was calculated for the perturbation zonal and vertical velocities at each vertical level, giving us a measure of the momentum flux associated with

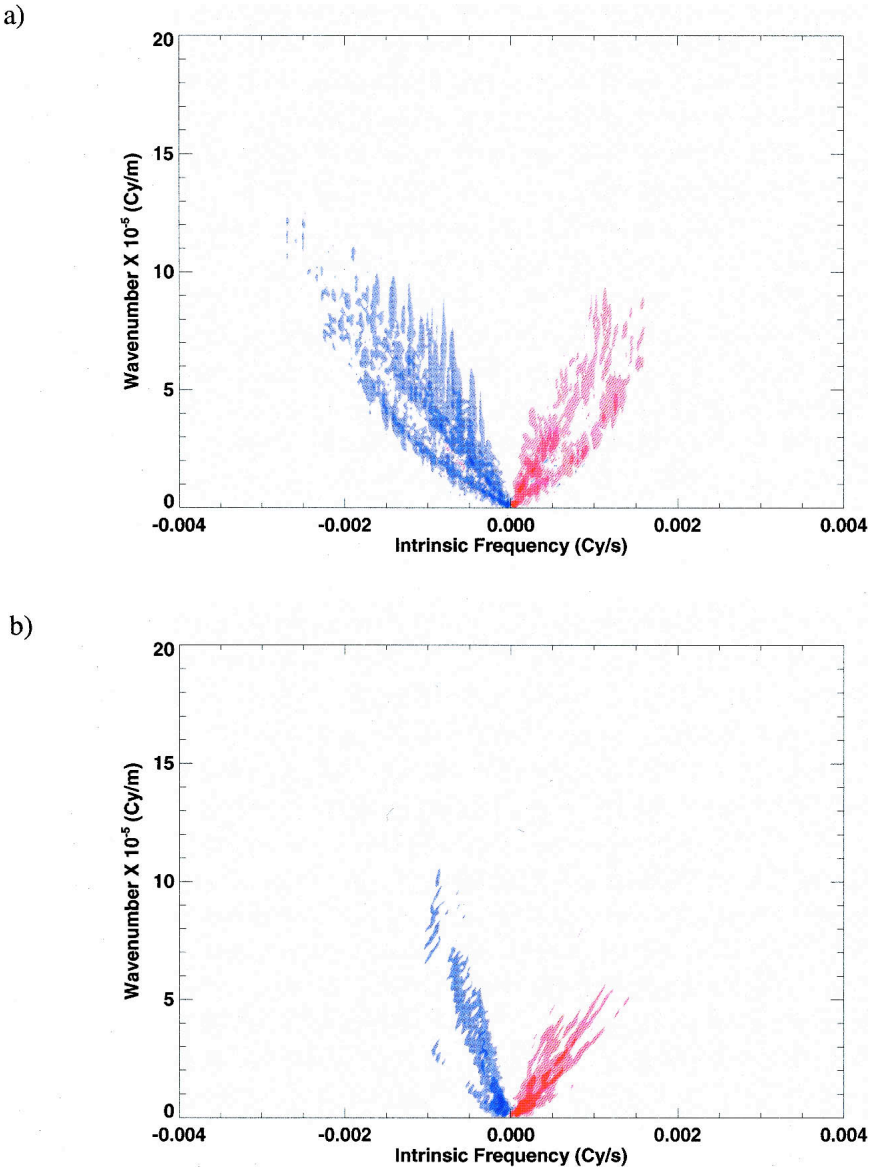

FIG. 14. Contour plot of the cospectra of horizontal and vertical velocity at 14 125 m as a function of horizontal wavenumber and intrinsic frequency for (a) the WK run and at 19 255 m for (b) the TC run. The red contours (0.000 01, 0.0001, 0.001, 0.01 $m^2 s^{-2}$) correspond to positive values of $\overline{u'w'}$, while the blue contours ($-0.000\,01$, -0.0001, -0.001, -0.01 $m^2 s^{-2}$) correspond to negative values of $\overline{u'w'}$. The zero contour is omitted.

each discrete wavenumber and frequency. We verified that the integral of these cospectra over all frequencies and wavenumbers was equivalent to the Eulerian mean momentum flux at the same vertical level averaged over time. A plot of the cospectrum in wavenumber and intrinsic frequency space is shown in Fig. 14a. In this plot, we see negative values of momentum flux associated with westward-propagating waves, and positive values of momentum flux associated with eastward-propagating waves, as we would expect. Also, the highest magnitudes of momentum flux are clustered along two lines of constant ω_{int}/k in both the negative and positive frequency ranges. We would therefore expect the momentum flux to be clustered around four intrinsic phase speeds ($\hat{c} \equiv \omega_{\text{int}}/k$).

A plot of the cospectrum of momentum flux at 19 255 m from the TC run is shown in Fig. 14b. While this figure does share some characteristics with Fig. 14a, there are also significant differences. The magnitude of the momentum flux produced by the TC run is smaller than that of the WK run.

We can calculate the amount of momentum flux associated with a bin of intrinsic phase speed between $\hat{c} - \Delta\hat{c}$ and $\hat{c} + \Delta\hat{c}$ by following the procedure of Alexander

and Holton (1997). We do this by adding up the amount of momentum flux from each point in (ω, k) space that falls within a given interval of phase speed. The results of such a calculation for the WK run, with $\Delta\hat{c}$ set to 1 m s^{-1}, are shown in Fig. 15a. We see that much of the negative momentum flux is associated with phase speeds between -10 and -30 m s^{-1}. There are also spikes at other negative (-50 m s^{-1}) and positive (15 and 25 m s^{-1}) phase speeds, which is similar to what we would expect from Fig. 14. There is very little momentum flux associated with waves with phase speeds greater than ± 50 or less than ± 10 m s^{-1}. The flat area in the spectrum at low phase speeds [also observed in Alexander and Holton (1997) and Piani et al. (2000)] can be understood by noting that waves that are close to an intrinsic phase speed of zero are preferentially damped, as shown in Lindzen (1981).

The spikes in the spectrum depicted in Fig. 15a at ± 25 m s^{-1} are partially associated with a mode that is an artifact of our use of periodic lateral boundary conditions. This "transient standing wave" mode has a wavenumber of 1 (associated with the antisymmetry in the sign of momentum flux in the domain), and a frequency of ± 1 (associated with the commencement of convection). Since the sizes of the space and time domains in our simulation are 900 000 m and 36 000 s, respectively, the transient standing wave mode shows up as a spike at ± 25 m s^{-1}. When the Fourier analysis is performed over shorter time periods (e.g., from 2 to 10 h), these spikes move to higher phase speeds, since the time domain has been reduced, while the rest of the spectrum remains relatively constant. Since we believe this mode to be a peculiarity of the specific domain size, analysis interval, and lateral boundary conditions of our simulation, the mode will be filtered in all subsequent presentations of the momentum flux spectra. The spectrum with this mode removed is shown in Fig. 15b. The transient standing wave mode is a contributor to the total eastward and westward momentum flux of the experiments, however, so the calculations of these quantities will contain the mode. Experiments where higher wavenumbers were removed revealed few additional differences in the momentum flux spectra.

After calculating the divergence of the momentum flux for the WK run, we found that the implied easterly acceleration of the lower portion of the model stratosphere would be under 1 m s^{-1} day^{-1}, which is somewhat consistent with the results of Alexander and Holton (1997; see their Fig. 8), although the upper portion of the model stratosphere has an implied easterly acceleration of up to 3 m s^{-1} day^{-1}. When the same calculation is performed on the TC run, the implied forcing of the mean wind is negative through the depth of the model stratosphere, but is less than 0.5 m s^{-1} day^{-1}, which is consistent with the results of Alexander and Holton (1997). The likely reason for the stronger implied mean flow forcing of the WK run is that the waves

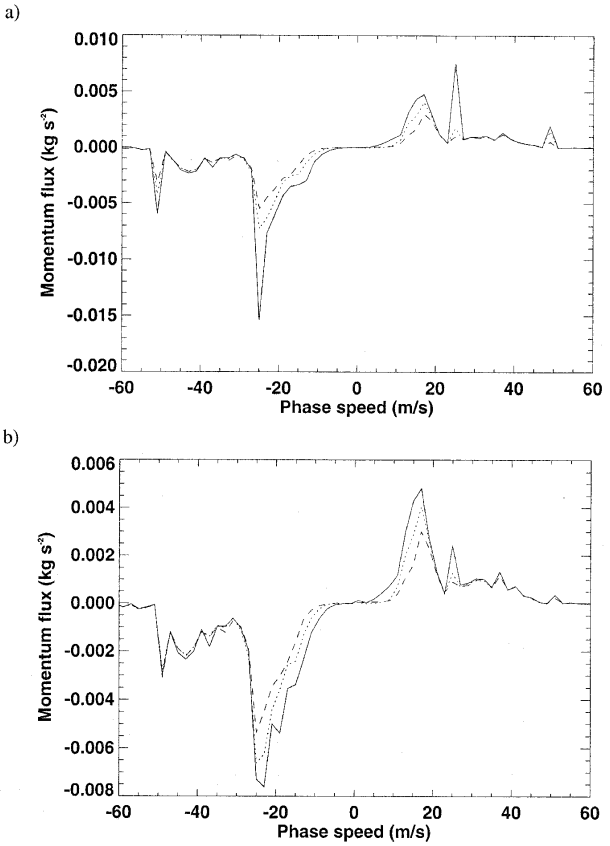

FIG. 15. (a) Plot of the momentum flux $\rho_0\overline{u'w'}$ at 14 125 m (solid), 21 125 m (dotted), and 28 125 m (dashed) as a function of horizontal intrinsic phase speed for the WK run. (b) As in (a), but with the k = 1, $\omega = \pm 1$ mode removed.

from that simulation had a stronger momentum flux to begin with.

The last case that we will examine is one that initially has zero wind throughout the atmosphere, with the same thermodynamic structure as the WK run. The momentum flux spectrum for this simulation is shown in Fig. 16b, and is quite symmetric, as one might expect with no environmental wind to alter the symmetry of the convection itself. In this simulation, there was an initial central updraft, which produced a cold pool that spread to the east and west, forcing convection at its two edges. The amplitude of the momentum flux is somewhat smaller than that of the WK run (cf. Fig. 15b), probably because the convection is less vigorous, as measured by the maximum vertical velocity.

Note that some previously published parameterizations of convectively generated gravity waves (Kershaw 1995; Chun and Baik 1998) would predict the momentum flux to be zero in the WK calm experiment. While this is true in terms of the net momentum flux, the offsetting eastward and westward momentum fluxes produced by these runs could be associated with significant mean flow accelerations if the waves were allowed to propagate upward into an environment with shear.

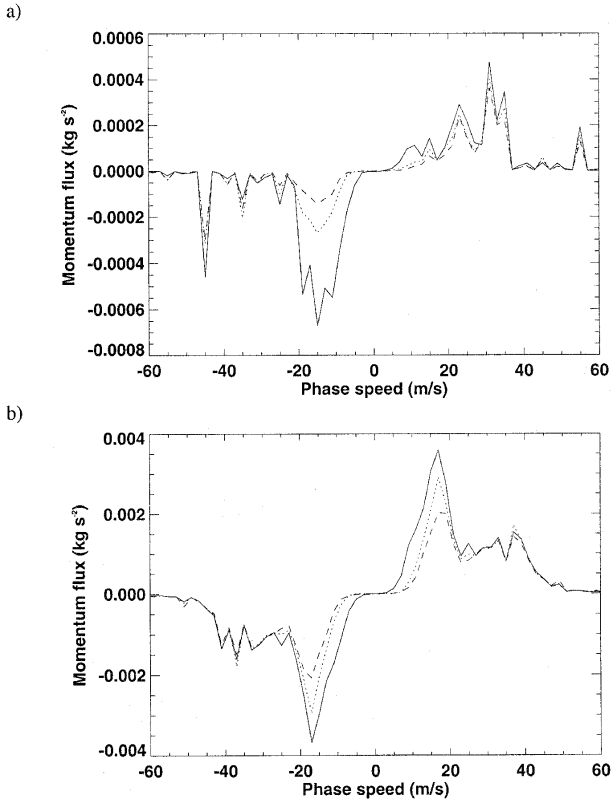

FIG. 16. Plot of the momentum flux $\rho_0\overline{u'w'}$ as a function of horizontal intrinsic phase speed (a) at 19 255 m (solid), 24 927 m (dotted), and 29 825 m (dashed) for the TC run and (b) at 14 125 m (solid), 21 125 m (dotted), and 28 125 m (dashed) for the WK calm run.

This indicates that a successful parameterization of convectively generated gravity waves needs to include multiple positive and negative phase speeds.

5. Coupling the stratosphere and troposphere

If we want to relate the wave energy flux $\overline{p'w'}$ to the wave momentum flux $\overline{u'w'}$, we can use the following Eliassen–Palm (1960) relationship for steady, linear gravity waves:

$$\overline{p'w'}(\hat{c}) = \rho_0 \hat{c}\,\overline{u'w'}(\hat{c}). \tag{11}$$

Here, $\hat{c}$ is the intrinsic phase speed, $c - \overline{u}$. The spectrum of wave momentum flux is treated as the input, and the wave energy flux is treated as the output. A test of the above relationship for the convectively generated waves is shown in Fig. 17. In this figure, we have taken the time-averaged (over the length of each simulation) Eulerian-mean $\overline{p'w'}$, and compared it to the rhs of (11) summed over all phase speeds for the WK and TC runs. The agreement is very good in the model stratosphere, but considerably worse in the model troposphere. Since we expect gravity waves to dominate the motion fields

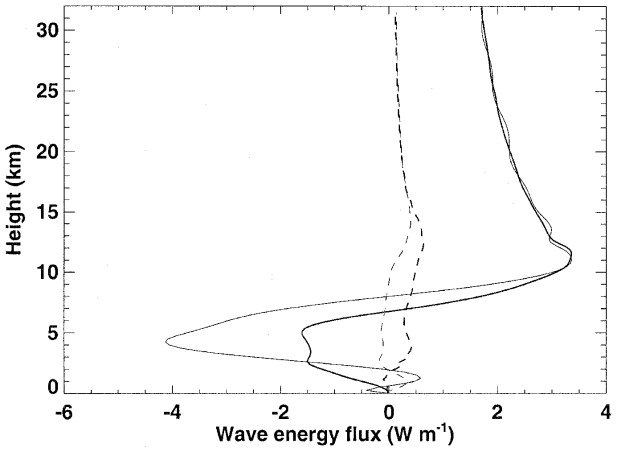

FIG. 17. Comparison of time-averaged Eulerian-mean wave energy flux (thin solid line) to a summation of the rhs of (11) (thick solid line) for the WK run, and the wave energy flux (thin dashed line) and a summation of the rhs of (11) (thick dashed line) for the TC run.

in the stratosphere but not the troposphere (where additional terms are important), this result makes sense. Note that (11) is also satisfied in the model stratosphere of several other simulations, as shown in Eitzen (2001).

When both the wave energy flux and wave momentum flux are accounted for, it is important to note that the total amount of wave energy flux associated with different momentum flux spectra can be quite different. In particular, a spectrum of $\overline{u'w'}(\hat{c})$ with an unrealistically high proportion of its power at high intrinsic phase speeds is associated with an unrealistically high amount of perturbation kinetic energy leaving the troposphere via vertically propagating gravity waves.

The prognostic equation for perturbation kinetic energy can be written as

$$\frac{\partial}{\partial t}\left(\frac{\rho_0\overline{u_i'u_i'}}{2}\right) + \frac{\partial}{\partial x_j}\left(\frac{\rho_0\overline{u}_j\overline{u_i'u_i'}}{2} + \frac{\rho_0\overline{u_j'u_i'u_i'}}{2} + \overline{p'u_j'}\right)$$
$$= \delta_{i3}\frac{\rho_0 g}{\overline{\theta}}\overline{u_i'\theta'} - \rho_0\overline{u_i'u_j'}\frac{\partial\overline{u}_i}{\partial x_j} + \varepsilon, \tag{12}$$

where ε represents dissipation and δ_{ij} is the Kronecker delta, equal to 1 when $i = j$, and 0 when $i \neq j$. Note that repeated indices imply summation of the x and z components (see Stull 1988). If we associate the perturbations in (12) with the circulations caused by moist convection inside a grid cell of a large-scale model, we can define the cumulus kinetic energy (CKE) as the vertical integral of the perturbation kinetic energy, or

$$K \equiv \int_{z_S}^{z_T} \frac{\rho_0\overline{u_i'u_i'}}{2}\,dz, \tag{13}$$

following Pan and Randall [1998; also Lord and Arakawa (1980)]. Here, z_T and z_S stand for the heights of the cloud top and the surface, respectively. If we ne-

glect horizontal transports, the vertical integral of (12) has the form

$$\frac{\partial K}{\partial t} = B + S - D - R - \mathrm{TM}, \tag{14}$$

where B represents the production of CKE by buoyancy

$$B = \int_{z_S}^{z_T} \delta_{i3} \frac{\rho_0 g}{\overline{\theta}} \overline{u_i' \theta'}\, dz, \tag{15}$$

S represents the production of CKE by shear

$$S = -\int_{z_S}^{z_T} \rho_0 \overline{u_i' u_j'} \frac{\partial \overline{u_i}}{\partial x_j}\, dz, \tag{16}$$

and D represents the viscous dissipation of CKE

$$D = \int_{z_S}^{z_T} \varepsilon dz. \tag{17}$$

The next term in (14) represents the energy loss due to the radiation of vertically propagating gravity waves (see Stull 1976), or

$$R = \overline{p'w'}(z_T). \tag{18}$$

Finally, TM represents the energy loss due to the triple-moment terms in (12)

$$\mathrm{TM} = \frac{\rho_0 \overline{u'u'w'}(z_T)}{2} + \frac{\rho_0 \overline{w'w'w'}(z_T)}{2}. \tag{19}$$

In Fig. 18, we compare the vertical profiles of R to the two terms in (19) for the WK run after being averaged from $t = 4$ to 6 h. We see from this figure that although the triple-moment terms are important in the troposphere, $\overline{p'w'}$ is dominant within the stratosphere. Similar results were obtained in the TC run. This indicates that the only important flux of energy out of the model troposphere is due to the wave energy flux.

The prognostic equation for the CKE of each subensemble in the Arakawa–Schubert cumulus parameterization as implemented by Pan and Randall [1998; also see Randall and Pan (1993)] is a representation of (14) with only the B and D terms, and is given by

$$\frac{\partial K(s)}{\partial t} = M_B(s)A(s) - D(s), \tag{20}$$

where s takes on different values for each subensemble, K is the CKE, A is the work done by each cloud element because of buoyancy, M_B is the mass flux into the cloud at its base, and D is the rate of dissipation of CKE. If we introduce a dissipation time scale τ_D for the CKE, (20) becomes

$$\frac{\partial K}{\partial t} = M_B A - \frac{K}{\tau_D}. \tag{21}$$

As Randall and Pan (1993) state, if A is defined to include the effects that liquid water and ice have on buoyancy, the dissipation term of (21) represents only the effects of true kinetic energy dissipation. Khairoutdinov and Randall (2002) have recently calculated values for τ_D in the range of 4 to 8 h, which is significantly longer than was previously thought (Lord and Arakawa 1980). However, additional terms on the rhs of (21) can be introduced that include the effects of vertically and horizontally propagating wave generation by the cumuli. The sign of a term for the vertically propagating waves will certainly be negative, as the waves represent energy produced by the convection that becomes lost to the middle and upper atmosphere where new moist convection cannot be generated. In the case of horizontally propagating waves, it is likely that at least some new convection may be triggered by the waves (Mapes 1993), causing these waves to potentially act as both sources and sinks of CKE. This is an interesting area for future research.

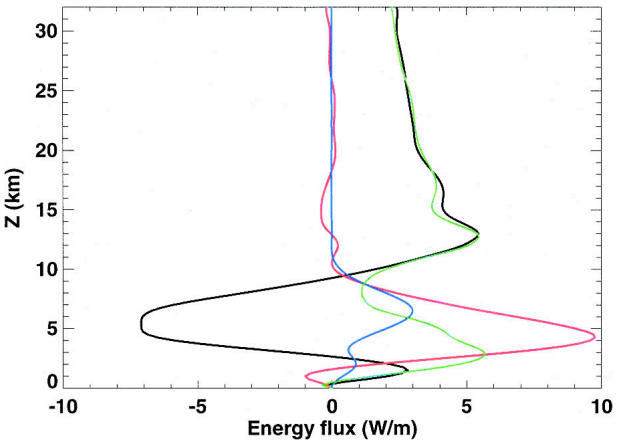

FIG. 18. Time-averaged energy fluxes due to $\overline{p'w'}$ (black line), $\rho_0\overline{u'u'w'}/2$ (red line), $\rho_0\overline{w'w'w'}/2$ (blue line), and their sum (green line) over hours 4–6 for the WK run.

If we focus on the effects of the vertically propagating waves, we might be tempted to introduce another term in the same form as the dissipation in (21) with a time scale τ_V associated with the vertically propagating waves:

$$R = -\frac{K}{\tau_V}. \tag{22}$$

An estimate of the time scale τ_V can be obtained by measuring the vertically integrated total perturbation kinetic energy of the troposphere in a mesoscale model that contains active convection, and then dividing this quantity by the wave energy flux $\overline{p'w'}$. A graph of this time scale for the TC and WK simulations is shown in Fig. 19. After the waves have had a change to propagate into the stratosphere, the time scale tends to oscillate around 10 h for the WK run, but is highly variable for the TC run. Note that these time scales are at least roughly comparable to the dissipation time scales calcu-

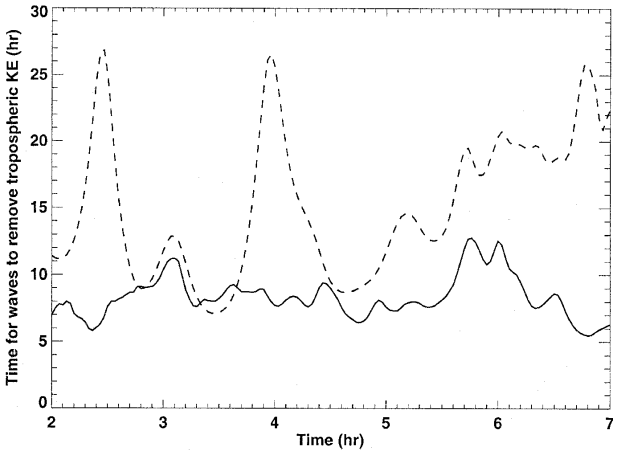

FIG. 19. Integrated perturbation kinetic energy of the troposphere divided by the wave energy flux at an altitude of 2 km above the model tropopause, at 14 km for the WK run (solid line), and 21 km for the TC run (dashed line) as a function of time.

lated by Khairoutdinov and Randall (2002). To account for this effect, a climate modeler could use a constant value for τ_V of perhaps 15 to 25 h judging from the TC run, which is probably more representative of convection in general than the WK run. However, a parameterization that assigns a realistic spectrum of momentum flux as a function of phase speed could then use (11) to calculate R. In addition, such a parameterization could realistically account for changes in the mean flow due to absorption of unresolved convectively generated gravity waves.

6. Conclusions

In this paper, we studied the generation of vertically propagating gravity waves by convection, as simulated by a two-dimensional numerical model. We applied several types of analysis to the simulated storms, the results of which are summarized below.

The trajectory analysis allowed us to divide the qualitative behavior of particles within the model troposphere into physically relevant categories such as moist updrafts, waves and turbulence, and subsidence. The behavior of the particles in the model stratosphere was consistent with what would be expected in the presence of high-frequency gravity waves. The thresholds used in the identification of updraft particles proved useful in determining criteria for the classification of updraft points in the conditional sampling analysis.

From the conditional sampling analysis, we found that the perturbation kinetic energy of the troposphere is dominated by horizontal motions, which is consistent with the results of Xu et al. (1992). The majority of the horizontal perturbation kinetic energy was found outside of the clouds, while a disproportionate amount of the vertical perturbation kinetic energy was confined within the points categorized as moist updrafts. We were also able to measure the difference between the horizontal velocity of the updrafts and the mean flow. This difference is a measure of the extent to which the updrafts act as an obstacle to the flow, and also relates to the convective momentum transport.

When we looked at the stratospheric waves in section 4, we found that convectively generated gravity waves cannot be accurately characterized by a single phase speed, since it is typical to see both eastward- and westward-propagating waves. This points to a problem with several existing parameterizations. The vertical wavenumber spectrum for the WK run indicates that the power peaks at a wavelength that is twice the depth of the convection, consistent with both theoretical (Salby and Garcia 1987) and modeling (PA99) results. The simulations with stronger convection tended to produce more wave momentum flux than those with weaker convection, as might be expected. Also, updrafts that propagate relative to the mean flow produce more waves that propagate in the same direction, which is consistent with the results of previous modelers as well as the modified Pfister et al. (1993) transient mountain hypothesis.

When we looked at the wave energy flux, we found that it is the sole important vertical flux of energy that extends into the stratosphere. When the wave energy flux is compared to that which would be predicted from the wave momentum spectrum, good agreement was found in the model stratosphere. This stratospheric sink of perturbation kinetic energy operates on a time scale that may be comparable to that of the dissipation time scale, indicating that the loss of CKE because of waves may be an important effect for modelers to take into account. We made suggestions as to how this effect could be parameterized.

In the future, much of the analysis in this work can be extended to fully three-dimensional studies. Also, more types of convection need to be analyzed, such as mesoscale convective complexes and leading stratiform squall lines. A parameterization has recently been developed (Cheng 2001) that can diagnose the type of MCS that is produced within a GCM grid cell, using information about the vertical wind shear and the moist Brunt–Väisälä frequency. The shapes of the MCSs could be related to momentum flux spectra by using transient mountains with similar shapes. The waves produced by shallower cumuli, which are ubiquitous in the Tropics, should also be studied.

In addition, the role of convective strength in producing gravity waves needs to be explored further. Also, the production of horizontally propagating gravity waves needs to be studied further, as these waves may also act as a sink to the CKE of an individual cloud, but may act as a source of CKE to another cloud (Mapes 1993). In addition, this study has not addressed other nonorographic sources of gravity waves such as shear, which may also be important. Finally, and per-

haps most importantly, more observational studies need to be made of convectively generated gravity waves.

Acknowledgments This research was supported in part by a grant from the National Science Foundation (ATM-9812384), and by grants from the U.S. Department of Energy (DE-FG03-95ER62102 and DE-FG03-98ER62611). We thank three anonymous reviewers for their helpful suggestions.

REFERENCES

Alexander, M. J., and J. R. Holton, 1997: A model study of zonal forcing in the equatorial stratosphere by convectively induced gravity waves. *J. Atmos. Sci.,* **54,** 408–419.

——, ——, and D. R. Durran, 1995: The gravity wave response above deep convection in a squall line simulation. *J. Atmos. Sci.,* **52,** 2212–2226.

Arakawa, A., and W. H. Schubert, 1974: Interaction of a cumulus cloud ensemble with the large-scale environment, Part I. *J. Atmos. Sci.,* **31,** 674–701.

Baldwin, M. P., and Coauthors, 2001: The quasi-biennial oscillation. *Rev. Geophys.,* **39,** 179–229.

Bretherton, F. P., 1969: Momentum transport by gravity waves. *Quart. J. Roy. Meteor. Soc.,* **95,** 213–243.

Cheng, A., 2001: A theory of the mesoscale organization of moist convection and the associated vertical momentum transport. Ph.D. dissertation, Colorado State University, 103 pp.

Chun, H.-Y., and J.-J. Baik, 1998: Momentum flux by thermally induced gravity waves and its approximation for large-scale models. *J. Atmos. Sci.,* **55,** 3299–3310.

Clark, J. H. E., and L. T. Morone, 1981: Mesospheric heating due to convectively excited gravity waves—A case study. *Mon. Wea. Rev.,* **109,** 990–1001.

Dewan, E. M., and Coauthors, 1998: MSX satellite observations of thunderstorm-generated gravity waves in midwave infrared images of the upper stratosphere. *Geophys. Res. Lett.,* **25,** 939–942.

Dunkerton, T. J., 1997: The role of gravity waves in the quasi-biennial oscillation. *J. Geophys. Res.,* **102,** 26 053–26 076.

Eitzen, Z. A., 2001: Simulation and parameterization of vertically propagating convectively generated gravity waves. Ph.D. dissertation, Colorado State University, 203 pp.

Eliassen, A., and E. Palm, 1960: On the transfer of energy in stationary mountain waves. *Geofys. Publ.,* **22**, 1–23.

Emanuel, K. A., 1994: *Atmospheric Convection.* Oxford University Press, 580 pp.

Fovell, R. G., D. R. Durran, and J. R. Holton, 1992: Numerical simulations of convectively generated stratospheric gravity waves. *J. Atmos. Sci.,* **49,** 1427–1442.

Fritts, D. C., and G. D. Nastrom, 1992: Sources of mesoscale variability of gravity waves. Part II: Frontal, convective, and jet stream excitation. *J. Atmos. Sci.,* **49,** 111–127.

Greenhut, G. K., and S. J. S. Khalsa, 1982: Updraft and downdraft events in the atmospheric boundary layer over the equatorial Pacific Ocean. *J. Atmos. Sci.,* **39,** 1803–1818.

Haertel, P. T., and R. H. Johnson, 2000: The linear dynamics of squall line mesohighs and wake lows. *J. Atmos. Sci.,* **57,** 93–107.

——, ——, and S. N. Tulich, 2001: Some simple simulations of thunderstorm outflows. *J. Atmos. Sci.,* **58,** 504–516.

Hartmann, D. L., cited 2004: ATM 552 notes. [Available online at http://www.atmos.washington.edu/~dennis/.]

Hines, C. O., 1960: Internal atmospheric gravity waves at ionospheric heights. *Can. J. Phys.,* **38,** 1441–1481.

Jorgensen, D. P., M. A. LeMone, and S. B. Trier, 1997: Structure and evolution of the 22 February 1993 TOGA COARE squall line: Aircraft observations of precipitation, circulation, and surface energy fluxes. *J. Atmos. Sci.,* **54,** 1961–1985.

Kershaw, R., 1995: Parameterization of momentum transport by convectively generated gravity waves. *Quart. J. Roy. Meteor. Soc.,* **121,** 1023–1040.

Kessler, E., 1969: On the Distribution and Continuity of Water Substance in Atmospheric Circulations. *Meteor. Monogr.,* No. 40, Amer. Meteor. Soc., 84 pp.

Khairoutdinov, M. F., and D. A. Randall, 2002: Similarity of deep continental cumulus convection as revealed by a three-dimensional cloud-resolving model. *J. Atmos. Sci.,* **59,** 2550–2566.

Klemp, J. B., and R. B. Wilhelmson, 1978: The simulation of three-dimensional storm dynamics. *J. Atmos. Sci.,* **35,** 1070–1096.

Krueger, S. K., G. T. McLean, and Q. Fu, 1995: Numerical simulation of the stratus-to-cumulus transition in the subtropical marine boundary layer. Part II: Boundary-layer circulation. *J. Atmos. Sci.,* **52,** 2851–2868.

Lane, T. P., M. J. Reeder, and T. L. Clark, 2001: Numerical modeling of gravity wave generation by deep tropical convection. *J. Atmos. Sci.,* **58,** 1249–1274.

LeMone, M. A., and E. J. Zipser, 1980: Cumulonimbus vertical velocity events in GATE. Part I: Diameter, intensity, and mass flux. *J. Atmos. Sci.,* **37,** 2444–2457.

Lin, C., and A. Arakawa, 1997: The macroscopic entrainment processes of simulated cumulus ensemble. Part I: Entrainment sources. *J. Atmos. Sci.,* **54,** 1027–1043.

Lin, Y.-L., R. D. Farley, and H. D. Orville, 1983: Bulk parameterization of the snow field in a cloud model. *J. Climate Appl. Meteor.,* **22,** 1065–1092.

Lindzen, R. S., 1981: Turbulence and stress owing to gravity wave and tidal breakdown. *J. Geophys. Res.,* **86,** 9707–9714.

Lord, S. J., and A. Arakawa, 1980: Interaction of a cumulus cloud ensemble with the large-scale environment. Part II. *J. Atmos. Sci.,* **37,** 2677–2692.

Mapes, B. E., 1993: Gregarious tropical convection. *J. Atmos. Sci.,* **50,** 2026–2037.

Nicholls, M. E., R. H. Johnson, and W. R. Cotton, 1988: The sensitivity of two-dimensional simulations of tropical squall lines to environmental profiles. *J. Atmos. Sci.,* **45,** 3625–3649.

——, R. A. Pielke, and W. R. Cotton, 1991: Thermally forced gravity waves in an atmosphere at rest. *J. Atmos. Sci.,* **48,** 1869–1884.

Pan, D.-M., and D. A. Randall, 1998: A cumulus parameterization with a prognostic closure. *Quart. J. Roy. Meteor. Soc.,* **124,** 949–981.

Pandya, R. E., and M. J. Alexander, 1999: Linear stratospheric gravity waves above convective thermal forcing. *J. Atmos. Sci.,* **56,** 2434–2446.

——, D. Durran, and C. Bretherton, 1993: Comments on "Thermally forced gravity waves in an atmosphere at rest." *J. Atmos. Sci.,* **50,** 4097–4101.

Percival, D. B., and A. T. Walden, 1993: *Spectral Analysis for Physical Applications: Multitaper and Conventional Univariate Techniques.* Cambridge University Press, 569 pp.

Pfister, L., W. Starr, R. Craig, M. Loewenstein, and M. Legg, 1986: Small-scale motions observed by aircraft in the tropical lower stratosphere: Evidence for mixing and its relationship to large-scale flows. *J. Atmos. Sci.,* **43,** 3210–3225.

——, S. Scott, M. Loewenstein, S. Bowen, and M. Legg, 1993: Mesoscale disturbances in the tropical stratosphere excited by convection: Observations and effects on the stratospheric momentum budget. *J. Atmos. Sci.,* **50,** 1058–1075.

Piani, C., D. Durran, M. J. Alexander, and J. R. Holton, 2000: A numerical study of three-dimensional gravity waves triggered by deep tropical convection and their role in the dynamics of the QBO. *J. Atmos. Sci.,* **57,** 3689–3702.

Randall, D. A., and D.-M. Pan, 1993: Implementation of the Arakawa–Schubert parameterization with a prognostic closure.

The Representation of Cumulus Convection in Numerical Models, Meteor Monogr., No. 46, Amer. Meteor. Soc., 137–144.

Redelsperger, J.-L., and Coauthors, 2000: A GCSS model intercomparison for a tropical squall line observed during TOGA-COARE. I: Cloud-resolving models. *Quart. J. Roy. Meteor. Soc.,* **126,** 823–863.

Reuter, G. W., and M. K. Yau, 1987: Mixing mechanisms in cumulus congestus clouds. Part II: Numerical simulations. *J. Atmos. Sci.,* **44,** 798–827.

Robe, F. R., and K. A. Emanuel, 2001: The effect of vertical wind shear on radiative-convective equilibrium states. *J. Atmos. Sci.,* **58,** 1427–1445.

Rotunno, R., J. B. Klemp, and M. L. Weisman, 1988: A theory for strong, long-lived squall lines. *J. Atmos. Sci.,* **45,** 463–485.

Salby, M. R., and R. R. Garcia, 1987: Transient response to localized episodic heating in the Tropics. Part I: Excitation and short-time near-field behavior. *J. Atmos. Sci.,* **44,** 458–498.

Sato, K., 1993: Small-scale wind disturbances observed by the MU radar during the passage of Typhoon Kelly. *J. Atmos. Sci.,* **50,** 518–537.

Schubert, W. H., 2000: A retrospective view of Arakawa's ideas on cumulus parameterization. *General Circulation Model Development,* D. A. Randall, Ed., Academic Press, 181–224.

Stull, R. B., 1976: Internal gravity waves generated by penetrative convection. *J. Atmos. Sci.,* **33,** 1279–1286.

——, 1988: *An Introduction to Boundary-Layer Meteorology.* Kluwer Academic, 670 pp.

Trier, S. B., W. C. Skamarock, M. A. Lemone, D. B. Parsons, and D. P. Jorgensen, 1996: Structure and evolution of the 22 February 1993 TOGA COARE squall line: Numerical simulation. *J. Atmos. Sci.,* **53,** 2861–2886.

Weisman, M. L., and J. B. Klemp, 1982: The dependence of numerically simulated convective storms on vertical wind shear and buoyancy. *Mon. Wea. Rev.,* **110,** 504–520.

Williams, C. R., W. L. Ecklund, and K. S. Gage, 1995: Classification of precipitating clouds in the Tropics using 915-MHz wind profilers. *J. Atmos. Oceanic Technol.,* **12,** 996–1012.

Xu, K.-M., A. Arakawa, and S. K. Krueger, 1992: The macroscopic behavior of cumulus ensembles simulated by a cumulus ensemble model. *J. Atmos. Sci.,* **49,** 2402–2420.

Xue, M., K. K. Droegemeier, and V. Wong, 2000: The Advanced Regional Prediction System (ARPS)—A multi-scale nonhydrostatic atmospheric simulation and prediction tool. Part I: Model dynamics and verification. *Meteor. Atmos. Phys.,* **75,** 161–193.

——, and Coauthors, 2001: The Advanced Regional Prediction System (ARPS)—A multi-scale nonhydrostatic atmospheric simulation and prediction tool. Part II: Model physics and applications. *Meteor. Atmos. Phys.,* **76,** 143–165.

Zipser, E. J., and M. A. LeMone, 1980: Cumulonimbus vertical velocity events in GATE. Part II: Synthesis and model core structure. *J. Atmos. Sci.,* **37,** 2458–2469.